Atmospheric teleconnection over Eurasia induced by aerosol radiative forcing during boreal spring

Maeng-Ki Kim
Dept. of Atmospheric Science, Kongju National University, Gongju, Korea

K. M. Lau
Laboratory for Atmospheres, NASA Goddard Space Flight Center, Greenbelt, Maryland, USA

Mian Chin
Atmospheric Chemistry and Dynamics Branch, Laboratory for Atmospheres, NASA GSFC, Greenbelt, Maryland, USA

Kyu-Myong Kim
Science System Applications, Inc, Lanham, Maryland, USA

Y. C. Sud
Climate and Radiation Branch, Laboratory for Atmospheres, NASA GSFC, Greenbelt, Maryland, USA

Greg K. Walker
SAIC/General Sciences Operation, Beltsville, Maryland, USA

Submitted to J. of Climate, March 2005

Corresponding author address: Dr. K. M. Lau, Laboratory for Atmospheres, NASA Goddard Space Flight Center, Code 910, Greenbelt, MD 20771, USA
E-mail: lau@climate.gsfc.nasa.gov

Abstract

The direct effects of aerosols on global and regional climate during boreal spring are investigated based on simulations using the NASA Global Modeling and Assimilation Office (GMAO) finite-volume general circulation model (fvGCM) with Microphyics of clouds in Relaxed Arakawa Schubert Scheme (McRAS). The aerosol loading are prescribed from three-dimensional monthly distribution of tropospheric aerosols *viz.*, sulfate, black carbon, organic carbon, soil dust, and sea salt from output of the Goddard Ozone Chemistry Aerosol Radiation and Transport model (GOCART). The aerosol extinction coefficient, single scattering albedo, and asymmetric factor are computed as wavelength-dependent radiative forcing in the radiative transfer scheme of the fvGCM, and as a function of the aerosol loading and ambient relative humidity.

We find that anomalous atmospheric heat sources induced by absorbing aerosols (dust and black carbon) excites a planetary scale teleconnection pattern in sea level pressure, temperature and geopotential height spanning North Africa through Eurasia to the North Pacific. Surface cooling due to direct effects of aerosols is found in the vicinity and downstream of the aerosol source regions, i.e., South Asia, East Asia, and northern and western Africa. Additionally, atmospheric heating is found in regions with large loading of dust (over Northern Africa, and Middle East), and black carbon (over South-East Asia). Paradoxically, the most pronounced feature in aerosol-induced surface temperature is an east-west dipole anomaly with strong cooling over the Caspian Sea, and warming over central and northeastern Asia, where aerosol concentration are low. Analyses of circulation anomalies show that the dipole anomaly is a part of an atmospheric teleconnection driven by atmospheric heating anomalies induced by absorbing aerosols in the source regions, but the influence was conveyed

globally through barotropic energy dispersion and sustained by feedback processes associated with the regional circulations. Atmospheric heating by dust aerosol over northern Africa and the Middle East is the primary driver of the atmospheric teleconnection, with significant contribution by black carbon over South and East Asia.

The surface temperature signature associated with the aerosol-induced teleconnection bears striking resemblance to the spatial pattern of observed long-term trend in surface temperature over Eurasia. Additionally, the boreal spring teleconnection pattern is similar to that reported by Fukutomi et al (2004) associated with boreal summer precipitation seesaw between eastern and western Siberia. The results of this study raise the possibility that global aerosol forcing during boreal spring may play an important role in spawning atmospheric teleconnection which affects regional and global climates.

1. Introduction

Recent studies have shown that aerosols may play an important role in determining the magnitude of global warming, because of their ability to alter the energy balance of the earth-atmosphere system through the interaction with solar and terrestrial radiation (e.g., Jacobson, 2001; 2002; Menon et al., 2002; Lohmann and Lesins, 2002). The effect of aerosols is not only limited to cooling by scattering, but also heating by absorption of solar radiation, depending on aerosol types. Because of their ability to deplete surface insolation from either scattering or absorption, all aerosols cause cooling at the earth surface. However, the sign of atmospheric temperature change induced by aerosol forcing can vary depending on the aerosol types, their elevation, and reflectivity of the underlying surfaces (Kaufman et al., 2002). Moreover, regional climate can also be influenced by circulation changes induced by aerosol radiative forcing. Thus aerosol-induced local heating and cooling, as well as the effects of induced circulation changes must be included in studies of climate responses to aerosol forcing.

For studies of global impact of aerosol on climate and water cycle, including feedback between forcing and response, a global climate models is a very useful, albeit imperfect tool. There have been numerous studies to estimate the direct and indirect effects of aerosol from optical and physical properties of clouds, and surface reflectivity, using global models, with idealized global aerosol forcings (Coakley and Cess, 1985; Chylek et al., 1995, 1996; Hansen et al., 1997; Quijano et al., 2000; Kay and Box, 2000; Weaver et al., 2002; Nishizawa et al., 2004; Cook and Highwood, 2004; Chung et al., 2002). However, relatively less attention has been devoted to studies of regional and global climate responses by three-dimensional aerosol radiative forcing, including feedback from atmospheric water cycle dynamics. Recently, a general circulation

model (GCM) simulation study by Menon et al. (2002) showed that there is a strong surface warming in remote regions of Eurasia, arising from regional sources of aerosols in China and India. However, model aerosol forcing and impacts have large uncertainties, primarily because of the inadequate representation of aerosol-cloud interaction physics, compounded by the poorly defined aerosol optical properties and vertical distribution (Hansen et al., 1997b). More recently, global aerosol transport models have successfully simulated, and validated against available observations, the three-dimensional climatological structure of aerosol distributions as well as their optical properties for various aerosol types (Chin et al., 2002; Chin et al., 2003; Takemura et al., 2002a, b). Outputs from these global aerosol models can be translated into more realistic, four-dimensional radiative forcing functions for GCM. This approach has been adopted in the present study.

In view of the inhomogeneous distribution of aerosol source, transports, associated thermal forcing and circulation changes, there can be no simple balance of aerosol, greenhouse gas, and dynamical forcing vis-á-vis regional climate change. For long-term climate change, almost all extratropical land regions show pronounced warming during boreal winter (IPCC 2001). However during boreal spring (April-May-June), both warming and cooling of extratropical land regions are noted. It has been suggested that the spring surface temperature pattern may be related to changes in large scale circulation, possibly related to aerosol effects. Fig.1 shows observed long-term mean boreal spring surface temperature anomaly (1961-1979 minus 1980-1998) for Africa and Eurasia.. Large areas of cooling appear in southern and eastern Asia, where aerosol loadings are known to be high. However, the most pronounced signal appears to be a dipole-like pattern with stronger surface cooling around the Caspian Sea, and warming

in the continental region around Baikal Lake. Yet, these two regions are located outside the large aerosol source regions, i.e., China, India, and Sahara. What then is the cause of this dipole-like temperature anomaly? Is remote forcing and large scale circulation changes induced by aerosols a contributing factor?

The aforementioned considerations have motivated us to investigate regional climate impact of global aerosol forcing on climate using a GCM, combined with more realistic global aerosol forcing derived from chemistry transport models. In this paper, we will limit to the "direct effect" of aerosols but including the full feedback involving large-scale circulation, clouds and convection. The investigation of "indirect effect" is an ongoing effort that is outside the scope of this work. Here, as a first step, we will focus on the boreal spring to identify possible signals of regional and global atmospheric response to aerosol forcing.. Boreal spring is chosen for this study, because it is the time of the year when a large number of land-based aerosol particles are injected into the atmosphere from biomass burning in southeast Asia, and Africa, from dust storms in the deserts Sahara and in northern Asia, as well as urban pollution in industrial regions of South and East Asia, and Europe (Takemura et al., 2000; Zhang et al., 2002; Kaufman et al., 2002; Novakov, 2003). These aerosols will have a longer residence time because wet deposition is at a minimum in boreal spring. In addition, dynamical forcings are also relative weak during the spring season compared to winter. Hence, thermally induced atmospheric responses by aerosol are more readily detectable. Moreover, the dynamical responses, in all likelihood, would pre-condition the evolving climate to influence the subsequent evolution of the anomalous summer monsoon.

The model and simulation experiments are described in section 2. In Section 3 and 4, we describe global aerosol forcing, global response, and possible mechanisms of

regional climate change. Section 5 discusses the special role of absorbing aerosols, i.e., black carbon and dust, on the regional change. The summary and additional discussions are presented in Section 6.

2. Model experiments

The climate impacts of aerosol radiative forcing are investigated using the NASA/GMAO finite volume General Circulation Model (fvGCM) with Relaxed Arakawa Schubert Scheme (McRAS). This version of the fvGCM has a horizontal resolution of 2 by 2.5 degrees and 55 vertical levels. The finite-volume dynamical core has a horizontal discretization built upon the flux-form semi-Lagrangian transport algorithms (Lin and Rood, 1996; Lin and Rood, 1997). The vertical structure is based on the Lagrangian control-volume concept (Lin, 1997). This alleviates some of the problems associated with sigma, pressure, or isentropic coordinates, thereby increasing the physical integrity and computational efficiency of the model (Chang et al., 2001). The McRAS microphysics cloud scheme was developed with the aim of parameterizing moist processes, microphysics of clouds, and cloud-radiation interactions in GCMs. It allows three cloud types: convective, stratiform, and boundary layer (Sud and Walker, 1999a; 1999b; 2003a, b). An evaluation of McRAS in a single-column model with the Global Atmospheric Tropical Experiment (GATE) Phase III data has shown that, together with the rest of the model physics, McRAS can simulate the observed temperature, humidity, and precipitation without discernible systematic errors (Sud and Walker, 1999a). The fvGCM is coupled to land surface model (Bonan 1996) and a planetary boundary model (Holtsage and Boville 1992). Radiative transfer model is described by Chou and Suarez (1999) and Chou et al. (2001). Aerosol optical

thicknesses of each of the five aerosols i.e., black carbon, organic carbon, dust, sulfate, and sea salt, are prescribed using three-dimensional monthly mean values for two years (2000 – 2001) from the Goddard Chemistry Aerosol Radiation and Transport (GOCART) model (Chin et al., 2002; 2003). The extinction coefficient, single scattering albedo (SSA), and asymmetric factor of each aerosol type are computed at 11 broad wavelength bands from Mie theory as a function of the ambient relative humidity. The optical parameters of dust are assumed to be a function of wave length only. Since aerosol interaction with long wave radiation is relatively small for most aerosols except for the large dust particles (e.g., Highwood et al., 2003), it is ignored in this study. The SSA used for dust is in the range i.e., 0.90- 0.92 at 0.55 μm averaged over the dust size bins, corresponding to moderate absorption. These values are higher than standard values used for fine dust (=0.8), but not as high as the value (~ 0.97) estimated by Kaufman et al (2001) for Sahara dust. The higher SSA value implies more absorbing aerosols. The value used here is deemed reasonable because absorption properties of air-borne dust in different parts of the world are likely to vary substantially, depending on the physical and chemical properties of the dust. Fine dust over Asia was found to be moderately absorbing with SSA=0.88 (Anderson et al. 2003). Moreover in Asia, and in some regions of Africa, air-borne dust particles are likely to be externally mixed with carbonaceous aerosols from industrial pollution, and biomass burning. Such a mixture is likely to have higher absorption (lower SSA) than pristine dust from the Sahara desert. As will be shown, it is not only the strength of the absorption, but rather the amount, extent and the high elevation of the dust lofted above by circulation and steep topography, that make dust an "effective" anomalous heat source in the atmosphere.

We have performed two 10-year long baseline model experiments, with all aerosols

(AA) from the GOCART model climatology, and one with no aerosols (NA). The sea surface temperature (SST) is prescribed using the weekly SST from September 1987 to December 1996 interpolated to daily values. All greenhouse gases and interactive land-atmosphere forcing are kept the same in both simulations. To assess the contributions of individual aerosol types and to delineate the nonlinear nature of the interaction between forcing and responses (Kondratyev, 1999), we carry out three additional model simulations, (which are otherwise identical to NA and AA); one without black carbon (NB), one without dust (ND), and one with dust only (OD).

3. Global Scale Response

a. Aerosol forcing

Fig 2 shows MAM mean distribution of aerosol optical thickness of all aerosols, dust and BC respectively, as provided by the GOCART climatology. The optical thickness of all aerosols (Fig.2a) shows that two major maximum are located over Northern Africa and East Asia, while two secondary maxima appear in Europe and Northeastern India. The elongated spatial pattern that extends from China to Japan reflects aerosol transport by the western Pacific subtropical high, a persistent circulation in the northern hemisphere during boreal spring and summer (Lau et al. 2000). Although the seasonal mean aerosol optical thickness is relatively low over the North America, it can be influenced by aerosols transported from Asia and Africa. Dust from the African continent is transported by upper level tropical easterlies to Central America and northern South America along the southern flank of high pressure system located in the Atlantic Ocean (Moulin et al., 1997; Kaufman et al., 2002). Even though wind and dust storms lift the dust in the arid regions, anthropogenic dust (disturbed soils) may

contribute up to 50% to the total atmospheric dust load (Tegen and Fung, 1995). The primary source of aerosols in central China is sulfates from industrial pollution, while in northern China it is dust from the Taklamakan and the Gobi Desert. In southern China, aerosols are made up of carbonaceous particles from biomass burning, industrial pollution, as well as desert dust from long-range transport (Fig. 2b, c). Aerosol optical thickness (AOT) in northeastern India/Bay of Bengal is mainly due to black carbon and organic carbon from industrial sources (Fig. 2c). In northern and northwestern Indian and Pakinstan, aerosols are lifted by wind storms from local deserts, as well as transport from Afghanistan, Middle East and North Africa. Conversely, in European and East Asian region, most carbonaceous particles are from industrial sources. The trend in global BC emission is quite non-linearly. In both United States and China, BC emissions have increased over the entire period 1950 to 1990 (Tegen et al., 2000). The spatial pattern of organic carbon (not shown) is similar to but its optical thickness is twice that of black carbon.

Fig.3 shows the monthly evolution of AOT of dust, carbonaceous, and sulfate aerosols in March through May. Dust aerosols over northern Africa appear to be most pronounced, with increasing concentration from March through May. Other regions that have high dust concentration include northern Indian Ocean, and northern China-Mongolia regions, where it contributes 60%-90% to the total AOT (Fig. 3a-c). The most important source of carbonaceous aerosols is biomass burning over northeastern India and the southeastern Asia during March through April (Fig. 3d-f). The carbon aerosols are reduced substantially, as a result of wet scavenging following the onset of the South China Sea monsoon in mid-May. Carbonaceous aerosols are also emitted from industrial regions with consumption of fossil and domestic fuels at a steady rate through

the year at midlatitudes of the Northern Hemisphere (Takemura et al., 2000), but they are in much smaller amount compared to those in south and southeast Asia. Large concentration of sulfate aerosols is found in East Asia and to a lesser extent, in Europe (Fig.3g-i). Sulfate is mainly formed in the atmosphere from the oxidation of SO_2, which is emitted predominantly from fuel combustions and industrial activities (Chin et al., 2002).

The effectiveness of aerosol forcing in producing far-field, global response is very much dependent on the height of the aerosol layer. Fig.4 shows the longitudinal average (0-150°E) latitude-height distribution of AOT of all aerosols, dust and black carbon, respectively. Two major sources are found over latitude 25-30° N and around 40° N, associated primarily with dust over the North Africa and inland desert, and sulfate and BC over Europe and China (Fig. 4a). Even at mid-to-high tropospheric level, the aerosol concentration remains considerable due to dynamic uplifting and transport. Fig.4b clearly shows most of aerosols at higher elevation are due to dust (mostly fine dust) which can be transported up and away from the source regions by the large scale circulation. In contrast, BC is most pronounced in the lower troposphere, from biomass burning and air pollution in low lying areas.

Fig.5 shows the aerosol radiative forcing induced by all aerosols in AA, at the top of the atmosphere (TOA), within the atmosphere (top-minus-surface), and at the surface respectively. The magnitude of aerosol radiative forcing at TOA is much smaller than that of the atmosphere or the surface. This is because the reflection of solar radiation by aerosols and clouds is largely offset by trapping of upwelling long wave radiation by clouds, so that the net radiation gain at the top of the atmosphere is small in comparison to its reduction at the surface (Miller and Tegen, 1998). The pattern of aerosol radiative

forcing of the atmosphere is similar to that of the surface but with the opposite sign, implying that if there is no aerosol in the atmosphere, the surface would have gained an amount equal to the atmospheric absorption. Table 1 shows that the globally averaged net radiation (shortwave and longwave) at the surface (-5.0 Wm^{-2}) is about three and half times larger than that at the top of the atmosphere (1.4 Wm^{-2}). The additional absorption by the atmosphere is about 3.6 Wm^{-2}. The definition of aerosol radiative forcing is somewhat arbitrary, because aerosol forcing depends upon column properties and these properties are modified by the forcing and the response (Miller and Tegen, 1998). For example, without perturbation to these fields by the dust forcing, global mean surface net radiative forcing in summer was estimated to be - 2.7 Wm^{-2} as computed by Miller and Tegen (1998). Yet, from the difference between two simulations, i.e., AA minus NA, the average reduction in the net radiation was roughly 10 Wm^{-2} over the extent of the dust cloud, which is defined as the region where the magnitude of the surface forcing is at least 5 Wm^{-2}. In this study, surface net radiative forcing due to dust-only is roughly - 5.6 Wm^{-2} over the northern hemisphere land (not shown). The difference between the two values is not large if the same area is considered. Surface radiative forcing by all aerosols in the annual mean is roughly -4.8 Wm^{-2}, which is similar to that of Jacobson (2001) but larger than that estimated by Hansen et al. (1997). Notice also that the depletion in surface shortwave (5.9 Wm^{-2}) is compensated by reduced longwave emission at the surface (0.9 Wm^{-2}), a gain in sensible (1.8 Wm^{-2}) and latent heat flux (1.5 Wm^{-2}), resulting in a smaller net energy loss at the surface (1.7 Wm^{-2}). Since globally evaporation must balance precipitation, the energy balance implies that there is a global reduction in precipitation equivalent to a lost of atmospheric heat of condensation of 1.5 Wm^{-2}, as a result of the adjustment of the atmospheric circulation

and associated changes in cloudiness and water vapor,.

Although not all aerosols absorb solar-radiation, the spatial distribution of atmospheric gain in radiative flux (net heating) is very similar to that of aerosol optical thickness. The atmospheric heating is mainly due to the contribution of black carbon and dust. Even though the optical thickness of black carbon is almost 10 times smaller than dust, the former plays a very important role in absorbing solar energy in the atmosphere, especially over East and South Asia (See Section 4 for more discussions). As suggested by Jacobson et al. (2001), the absorption power of solar radiation by black carbon may be potentially larger than that of the model simulation. It is because black carbon can exist in one of several possible internally or externally mixing states which have different and stronger absorption compared to pure carbon (Haywood et al., 1997; Jacobson, 2000).

b. Dynamical responses

Fig.6 shows the aerosol induced (AA minus NA) temperature anomalies at 850 hPa and 500 hPa. The most prominent feature is a wavetrain pattern in the lower and middle layer of the troposphere emanating from the Sahara region, through Europe, Siberia into northeastern Asia. Large positive anomaly can be seen over northern Africa and the Mediterranean, accompanied by negative anomaly over Europe. Over western and northern Asia, where aerosol loading is relatively low, the magnitude of temperature changes are larger than those found at the source regions, e.g.,. central China, which shows strong low tropospheric cooling caused by sulfate aerosols. At 500hPa, the pattern (Fig.6b) shows a pronounced elongated "warm bridge" extending from central Asia to North America coupled with weak cooling to the south. While portions of the warm bridge over North Africa, South Asia and East Asia lie within the aerosol source

regions, large signal-to-noise ratio (larger than 5% confidence level shown as shaded) appear mainly outside these regions. The wavetrain resembles the steady state response of the atmosphere to thermal and orographic forcing via Rossby wave energy dispersion (Hoskins and Karoly, 1981). The above results suggest that the wavetrain pattern is induced by circulation rather than due to to direct aerosol radiative forcing.

The large scale circulation changes induced by aerosol direct forcing can be seen clearly in the sea level pressure (SLP) and 500 hPa geopotential height anomalies, as shown in Fig. 7. Large positive SLP anomaly is found over East Asian monsoon region with the center around the Korean peninsula while negative anomaly is found over Tibetan Plateau, forming an east-west dipole pattern. The latter is mainly due to surface warming induced by surface albedo-aerosol interaction associated with aerosols absorbing multiply scattered solar radiation over the high surface albedo of the Tibet Plateau (Bakan et al., 1991; Quijano et al., 2000; Takemura et al., 2002a). The geostrophic southwesterlies associated with the SLP anomaly over the North Pacific will cause warm advection toward the central and northern part of Asian continent, which may be responsible for the surface warming shown in Fig.6. This pattern also implies a strengthening of the western Pacific subtropical high, which governs the onset and evolution of the East Asian summer monsoon. Large SLP anomalies are also found in the Africa-European region with the positive SLP north of the Mediterranean Sea, and negative SLP over North Africa. The previously described cooling around the Caspian Sea (Fig.6) may be explained in terms of the southward cold advection induced by anticyclonic flow around the European High. The circulation change in the mid troposphere (Fig. 7b) is in agreement with the temperature change shown in Fig.6b. In the mid troposphere, the cold trough appears to be more significantly around the

Caspian Sea than in the lower troposphere.

4. Regional responses

In this section, we discuss the regional circulation associated with the aforementioned teleconnection induced by aerosol forcing, focusing on the East Asian, and the North Africa/Europe sectors.

a. East Asian region

In boreal spring, the climatological convergence zone in East Asia is located around the latitude 30°N (Fig. 8a), coinciding with a region of high aerosol concentration, primarily sulfate, but with significant contribution from dust and BC (Fig. 8c). In the southern part of this region, carbonaceous aerosols are abundant, while in the northern part, dust aerosols dominate (Fig. 8c). The direct surface cooling due to aerosol is obvious in the large negative surface temperature anomaly in the region 20-40°. In spite of the complex aerosol loading pattern in this region, the circulation change by meridional wind shows clearly reversed pattern, associated with suppression of convection in the mean convergence zone, compared to the control (Fig. 8b). The suppression is due to the increase of static stability associate with warming of the lower troposphere and cooling of the surface due to aerosols (Fig. 8c), i.e., the semi-direct effect (Hansen et al. 1997). The reduced latent heating, associated with suppressed convection, coupled with surface cooling and turbulent mixing within the boundary layer produce a negative temperature anomaly that extends from the surface to the entire troposphere (Fig.9a). The suppressed convection in addition, induces a complex local circulation, as shown in the anomalous vertical motion field (Fig. 9d). In the convergence zone around 30°N where sulfate aerosol loading is significantly large, anomalous descent is induced, i.e., the climatological upward motion is weakened.

However ascending motion is induced north and south of this zone, where dust and BC concentrations respectively are relatively high. As shown in Fig. 9b, the shortwave heating due to aerosol is slightly larger in the outer part of convergence zone than within. Hence, this heating will provide a positive feedback due to the reinforced rising motions outside the convergence zone. As shown in Fig. 9a, large atmospheric warming is found in the latitude belt 40 – 60° N, where shortwave heating by aerosol is relatively weak. Fig. 9c shows that diabatic cooling stemming from reduced condensation heating is dominant in this region. However, in 40-60° N, adiabatic warming due to downward motion is more important in maintaining the large tropospheric warming there. Overall, it is clear that the response is complex and far from a simple pattern linked to direct aerosol forcing in the source regions. The structure and magnitude of the regional response is determined by the balance between shortwave heating and induced condensation heating/cooling, as well as adiabatic effects, and turbulent diffusion in the boundary layer.

b. Africa-Europe region

Similar to the East Asian region, the initial aerosol direct forcing induces a complex regional response, involving feedback of the atmospheric water and energy cycles in the North Africa – Europe sector. Here, the climatological meridional convergence zone is located at the southern boundary of the desert region of North Africa, near 10° N (Fig. 10a). Fig. 10 c, shows that dust aerosol dominate North Africa, 5-35°N, while sulfate is relatively abundant over Europe, 40-60° N. The BC concentration is generally low, with a slight maximum near 5° N and 50° N. The convergence is weakened by aerosol effects as seen in the induced anomalous meridional circulation (Fig. 10b), and the

surface cooling due to aerosol direct effect near 10°N (Fig. 10c). The surface cooling extends into the lower troposphere up to 750 hPa (Fig. 11a), but the shortwave heating by dust extends up to 500 hPa, thus giving rise to positive temperature anomaly above 700 hPa. The semi-direct effect is evident in the differential vertical heating, which increases the vertical stability of the atmosphere leading to reduced convection and anomalous sinking motion (Fig. 11d). Over the desert region (20 -30°N), slight surface warming is found (Fig. 10c). This is because absorbing aerosol over a high-albedo surface can produce multiply reflected solar radiation between the dust layer and the surface, producing warming that offsets most of surface cooling induced by aerosol scattering and absorption in the atmosphere. As a result, anomalous upward motion is induced by shortwave heating by the abundant dust aerosol above the boundary layer, and reinforced by positive feedback from the anomalous meridional circulation. Consequently, the latitudinal distribution of surface air temperature does not correspond to that of the AOT distribution (Fig. 10c).

Shortwave heating by aerosols is large over Saharan region 10–30° N, and small over the European region, 40-60 N (Fig. 11b). The vertical range of aerosol loading in Saharan and European region, reaches at least to the middle troposphere, implying that dust and black carbon aerosol are lifted over the height of planetary boundary layer (PBL) with the range from 800 to 1500m in Saharan region (~ 850hPa level). On the other hand, in the Mediterranean belt, 30-40N, shortwave heating is very weak, because this region is not located in the main track of aerosol transport in the spring. The temperature anomaly pattern shown in Fig.11a does not correspond to shortwave radiative heating but reflects the role of induced diabatic heating (Fig.11c), associated with the dynamic responses. As shown in Fig. 11c, diabatic cooling is, almost -

0.5K/day, significant in the lower troposphere at 10°N, where negative temperature anomaly is found. This is because aerosols reduce the net solar flux reaching the surface, and consequently reduces the planetary boundary layer (PBL) height. In this way turbulent mixing causes reduced PBL height and negative temperature anomaly in the lower troposphere. When absorbing aerosols such as smoke and mineral dust are lifted over the PBL by penetrative convection and long-range transport, they can increase the strength of capping inversion, which, in turn, cools PBL, and reduces the PBL height. Our analysis (not shown) that maximum cooling rate by vertical diffusion is about -1.0 K/day in this region.

As shown in Fig. 11d, the induced meridional circulation features enhanced upward motion, coupled with low SLP (see Fig.7a) and increased tropospheric temperature (Fig.11a) in the northern part of the Saharan (20-30° N). In the upper troposphere between 30-40°N, air-mass is transported northward (Fig. 10b). As the airmass goes northward, it cools and sinks at the latitude of 50° N (Fig. 11d), consistent with the development of the SLP high over Europe (See Fig. 7a). The results indicate that the anomalous meridional overtuning associated with interaction of atmospheric heating and surface cooling near the aerosol source region is critical in setting up the downstream teleconnection pattern outside the region of aerosol forcing.

5. Relative roles of dust vs. black carbon

In this section, we present results from additional experiments to demonstrate the relative importance of the two dominant absorbing aerosols, i.e. dust and black carbon, in contributing to the boreal spring teleconnection. Fig. 12 shows the MAM atmospheric gain in radiative flux (top-minus-bottom), based on an experiment where

the forcing from dust aerosol is withheld (ND), and another one where BC forcing is withheld (NB). In ND, almost all the atmospheric radiative heat gain is concentrated over the South Asia and Southeast Asia monsoon region, and to a smaller extent in northeastern Europe, where BC and sulfate are dominant. On the other hand, in NB, the atmospheric radiative heat gain is confined over northern Africa and the Middle East, where the subtropical deserts are located.

To show the relative impacts of dust and BC, we have constructed the difference maps of AA-minus-ND (for dust) and AA-minus-NB (for BC), and compared them to the full aerosol impact (AA-minus-NA). The tacit assumption here is that the present-day climate is associated with AA, and we examine the impacts of dust, and BC, by asking the questions what if dust or BC were missing?

Fig. 13 shows the surface air-temperature anomalies for the three cases. The statistical confidence here is computed as a two-tailed student's t-test, based on the 10 independent samples, i.e, 10 seasons, subject to the same aerosol forcings. With all-aerosol forcing (Fig. 13a), the most pronounced (exceeding 1% confidence level) surface cooling is found in a broad region over the Caspian Sea, which however, is not a region of high aerosol loading. Hence the strong cooling here is not due to direct radiative effect of aerosols, but rather a response to in the large-scale circulation (See discussion in Section 3b). In contrasts, the negative anomalies found over the aerosol source region of the Bay of Bengal (BC), East Asia (BC and sulfate), and western Africa (dust) are consistent with the direct forcing by aerosols. The strongest surface warming is found over an extensive region in northeastern Asia is far from the aerosol source regions, and opposite in sign that that expected from aerosol forcing. The surface warming over the northern India is apparently due to the BC and dust aerosol

stacking up against the southern slope of the Himalayas, acting as an elevated heat source. Here the surface rapidly rises to 3-5 km above sea level. The elevated aerosol heat source leads to anomalous warming of the upper troposphere in late spring, and consequently causes enhanced increased rainfall over northern India and the Bay of Bengal during the following summer. The impacts of aerosols on the South Asian monsoon is a subject of a separate paper (Lau and Kim, 2005).

Figure 13a shows a broad region of surface warming over southern Europe which, as shown below, is found to be a part of a wavetrain signal forced by dust aerosol over northern Africa. From Fig. 13b, it is obvious that the pronounced cooling over eastern Europe and the Caspian Sea region is associated with an atmospheric teleconnection forced by dust aerosol heating over northern and western Africa. This wavetrain produces warming over southern Europe, and northern Siberia. As shown in Fig. 13c, BC produces surface cooling over eastern India and East Asia, and in doing so induces a meridional circulation over the East Asian sector (see discussion in Section 4a) with strong subsidence in northern latitudes (40-60^{0} N). The most pronounced effect is to enhance the surface warming over central and eastern Siberia.

The signature of atmospheric teleconnection induced by dust and BC from the source region is also evident in the 500hPa geopotential height anomalies for the NA, ND and NB experiments shown in Fig. 14. From Fig. 14b, it is clear that dust over northern Africa and the Middle East induces a trans-continental wavetrain spanning northwestern Europe across Siberia to northeastern East Asia. This wavetrain appears to reproduce the polar component (north of 40^{0} N) of the wavetrain due to radiative forcing by all aerosols (Fig. 13a), suggesting the primary importance of dust aerosol in forcing the teleconnection. The negative anomaly associated with tropospheric cooling

north of the Caspian Sea is very prominent. In contrast, the contribution of BC forcing to the atmospheric teleconnection is manifested in increasing the magnitude and area of large positive height signal over eastern Siberia (Fig. 14c). Comparing Figs. 13 and 14, and 200 hPa anomalies (not shown) the wavetrain signal is quasi-barotropic, with a vertical structure that extends from the surface to the upper troposphere.

Because of nonlinear interactions among the changes in diabatic heating and circulation, the sum of the influences of all the aerosols is not equal to the effects of the sum of the individual contributions (Kondratyev, 1999). These results reaffirm that the two key absorbing aerosols (dust and BC) can contribute to regional climate anomalies not only through direct radiative forcing but also through interaction of diabatic heating (radiative and latent heat of condensation) associated with the anomalous circulation.

6. Discussion and conclusions

Experiments with the NASA fvGCM show that global aerosol radiative forcing in boreal spring can induce an atmospheric teleconnection pattern, with pronounced signatures in sea level pressure, surface temperature, and geopotential height, that spans northern Africa, southern Europe, Siberia and northeastern Asia. Surface cooling is found in the vicinity and downwind of source regions over South and East Asia, West Africa and Europe, consistent with the "direct effect" of aerosol forcing. However, the most pronounced surface temperature feature is a dipole-like anomaly with cooling found near the Caspian Sea, and warming north of Lake Baikal. The dipole anomalies are located over regions where aerosol forcing is weak, and arise from remote dynamical response induced by aerosol forcing, enhanced by local circulation feedback.

In the Africa-European region, low pressure anomaly develops as a result of direct

atmospheric heating by Saharan dust in the lower and middle troposphere. The heating enhances upward motion in the Saharan region and drives an anomalous meridional cell with downward motion, high pressure and surface warming over southern Europe. Through barotropic dispersion (Karoly and Hoskins, 1981), atmospheric energy propagates away from the source region eastward over Europe, across Siberia to the North Pacific. The cooling at the Caspian Sea is not due to direct aerosol heating, but rather associated with the southward advection of cold air from high latitudes on the eastern side of the surface pressure anomaly over Europe. Similarly, over East Asia region, BC aerosol induces a multi-cellular meridional overturning, with sinking motion over central and northeastern Asia (50-70^{o} N), which lead to adiabatic warming. The warming is enhanced by advection from the western side of the anomalous West Pacific High, which is a part of the atmospheric teleconnection pattern.

We find that the springtime atmospheric teleconnection is primarily caused by dust aerosol over North Africa, with reinforcement due to BC aerosol forcing over South and East Asia. The result also implies that strong atmospheric heating by absorbing aerosols can redistribute energy over the broad regions far away from the source regions. The springtime atmospheric teleconnection pattern is excited due to the interaction of atmospheric dynamics and diabatic heating processes in the atmosphere, driven by atmospheric heat sources associated with dust and BC aerosol loading.

Our results should provide useful clues for extracting signals of climate response to aerosol forcing from . In the real world, the atmospheric teleconnection simulated by the model may be interpreted as a signal of interannual climate anomalies generated by episodes of strong dust storms over North Africa and the Middle East region during boreal spring. It is also interesting to note that the surface air temperature anomalies

induced by global aerosol (Fig. 13a) is quite similar to the long-term trend pattern shown in Fig. 1, except for the West Africa sector, which has the opposite sign. This may lead to the hypothesis that direct aerosol forcing, perhaps from increasing BC emission trend in the last several decades may have played a role in the observed long-term temperature dipole over Eurasia. Similarly, the 500 hPa, and 850hPa temperature anomaly patterns shown in Figs. 14a, b bear strong resemblance to the teleconnection associated with anomalous storm track activities over Eurasia and a summertime precipitation seesaw between western and eastern Siberia (Fukutomi et al. 2004), suggesting that summertime rainfall seesaw may have been pre-conditioned by enhanced atmospheric heating dust aerosol over northern Africa and the Middle East. Clearly further observation and modeling studies are needed to validate these hypotheses.

Acknowledgments

This work is supported by the NASA Modeling and Analysis Program. Most of the work was carried out while the first author is visiting the Laboratory for Atmospheres, on a joint GSFC and Goddard Earth Sciences and Technology Center (GEST) fellowship. M. K. Kim was partially supported by the SRC program of Korea Science and Engineering Foundation.

References

Anderson, T.L., S. J. Masonis, D. S. Covert, N. C. Alquist, 2003: Variability of aerosol optical properties derived from in-situ aircraft measurements during ACE-Asia. J. Geophys. Res., 108, D23, 8647, doi:10.1029/2002JD00347.

Bakan, S., and Coauthers, 1991: Climate response to smoke from the burning oil wells in Kuwait. Nature, 351, 367-371.

Bonan, G. B., 1996: A land surface model (LSM version 1.0) for ecological hydrological, and atmospheric studies: technical description and user's guide. NCAR tech. Note NCAR/TN-417+STR, 150 pp.

Chang, Y., S. D. Schubert, S.-J. Lin, S. Nebuda, and B-W. Shen, 2001: The climate of the FVCCM-3 model. NASA/TM2001-104606, Vol. 20, 127p.

Chin, M., P, Ginoux, S. Kinne, O. Torres, B. N. Holben, B. N. Duncan, R. V. Martin, J. A. Logan, A. Higurashi, and T. Nakajima, 2002: Tropospheric Aerosol Optical Thickness from the GOCART Model and Comparisons with satellite and Sun photometer Measurements, J. Atmos. Sci., 59, 461-483.

Chin, M., P. Ginoux, R. Lucchesi, B. Huebert, R. Weber, T. Anderson, S. Masonis, B. Blomquist, A. Bandy, and D. Thornton, 2003: A global aerosol model forecast for the ACE-Asia field experiment, J. Geophys. Res., 108 (D23), 8654, doi:10.1029/2003JD003642.

Chou, M.-D. and M. Suarez, 1999: A solar radiation parameterization for atmospheric studies. NASA/TM-1999-104606, Vol. 15, 40p

Chou, M.-D., M. Suarez, X.-Z. Liang, and M. M.-H. Yan, 2001: A thermal infrared radiation parameterization for atmospheric studies. NASA/TM-2001-104606, Vol. 19, 56p

Chung, C.E., Ramanathan, V., and Kiel, J., 2002: Effects of south Asian absorbing aerosol haze on the northeast monsoon and surface-air heat exchange. J. Climate, 15, 2462-2476.

Chylek, P., G. Videen, D. Ngo, and R. G. Pinnick, 1995: Effect of black carbon on the optical properties and climate forcing of surface aerosols. J. Geophys. Res., 100 (D8), 16325-16332.

Chylek, P., G. B Lesin, G. Videen, J. G. D. Wong, R. G. Pinnick, D. Ngo, and J. D. Klett, 1996: Black carbon and absorption of solar radiation by clouds. J. Geophys. Res., 101 (D18), 23365-23371.

Coakley, J. A. and R. Cess, 1985: Response of the NCAR community climate model to the radiative forcing by the naturally occurring tropospheric aerosol. J. Atmos. Sci., 42, 1677-1692.

Climate Change 2001: The Scientific Basis. Contribution of Working Group I to the Third Assessment Report of the IPCC., Ed. J. T. Houghton *et al*, Cambridge University Press, 867pp

Hansen, J., M. Sato, A. Lacis, and R. Ruedy, 1997a: Radiative forcing and climate response. J. of Geophys. Res., 102(D6), 6831-6864.

Hansen, J., M. Sato, A. Lacis, and R. Ruedy, 1997b: The missing climate forcing. Phil. Trans. R. Soc. Lond. 352, 231-240.

Haywood, J.M., D. L. Roberts, A. Slingo, J. M. Edwards, and K. P. Shine, 1997: General circulation model calculations of the direct radiative forcing by anthropogenic sulfate and fossil-fuel soot aerosol. J. Climate, 10, 1562-1577.

Highwood, E. J., Haywood, J., Silverstone, M., Newman, S., and Taylor, J., 2003: Radiative properties and direct effect of Saharan dust measured by the C-130

aircraft during SHADE. 2. Terrestrial spectrum. J. Geophys. Res., 108, D18, 8578, doi:10.1029/2002JD002552.

Holtslag, A. A. M., and B. A. Boville, 1993: Local versus nonlocal boundary-layer diffusion in a global climate model. J. Climate, 6, 1825-1842.

Hoskins, B. J., and D. J. Karoly, 1981: The steady state response of a spherical atmosphere to thermal and orographich forcing. J. Atmos. Sci., 38, 1179-1196.

Hsu, N. C., J.R. Herman and S. C., Tsay, 2003: Radiative impacts from biomass burning in the presence of clouds during boreal spring in the Southeast Asia. Geophys. Res. Lett., 30(5), 1224, doi:10.1029/2002GL016485.

Jacobson, M., 2001: Strong radiative heating due to the mixing state of black carbon in atmospheric aerosols. Nature, 409, 695-697.

Jacobson, M. Z., 2002: Control of fossil-fuel particulate black carbon and organic matter, possibly the most effective method of showing global warming. J. Geophys. Res., 2002, 107, D19, doi:10.1029/2001JD001376.

Kaufman, Y. J., D. Tanre, and O. Boucher, 2002: A satellite view of aerosols in the climate system. Nature, 419, 215-223.

Kaufman, Y., et al: SSA of Sahara dust

Kay, M. J. and M. Box, 2000: Radiative effects of absorbing aerosols and the impact of water vapor. J. of Geophys. Res., 105(D10), 12221-12234.

Kondratyev, K. Y., 1999: Climatic effects of aerosols and clouds. Praxis Publishing, UK, 264pp.

Lau, K.-M., K.-M. Kim, and S. Yang, 2000: Dynamic and boundary forcing characteristics of regional components of the Asian summer monsoon. J. Climate, 13, 2461-2482.

Lin, S.-J., 1997: A finite-volume integration method for computing pressure gradient forces in general vertical coordinates. Q. J. Roy. Met. Soc., 123, 1749-1762.

Lin, S.-J. and R. B. Rood, 1997: An explicit flux-form semi-Lagrangian shallow water model on the sphere. Q. J. Roy. Met. Soc., 123, 2477-2498.

Lin, S.-J. and R. B. Rood, 1996: Multidimensional flux form semi-Lagrangian transport scheme. Mon. Wea. Rev., 124, 2046-2070.

Lohmann, U. and G. Lesins, 2002: Stronger constraints on the anthropogenic indirect aerosol effect. Science, 298, 1012-1015.

Menon, S., J. Hansen, L. Nazarenko, and Y. Luo, 2002: Climate effects of black carbon aerosols in China and India. Science, 297, 2250-2253.

Miller, R. L. and I. Tegen, 1998 Climate response to soil dust aerosols. J. of. Climate, 11, 3247-3267.

Moulin C. et al., 1997: Control of atmospheric export of dust from North Africa by the North Atlantic oscillation. Nature, 387, 691-694.

Nakagima, T., M. Sekiguchi, T. Takemura, I. Uno, A. Higurashi, D. Kim, B. J. Sohn, S.-N. Oh, T. Y. Nakajima, S. Ohta, I. Okada, T. Takemura, and K. Kawamoto, 2003: Significance of direct and indirect radiative forcing of aerosols in the East China Sea region. J. Geophys. Res., 108(D23), 10,1029/2002JD003261.

New, M., M. Hulme, and P. Jones, 2000: Representing twentieth-century spae-time climate variability. Part II: Development of 1901-96 monthly grids of terrestrial surface climate. J. Climate, 13, 2217-2238.

Nishizawa, T., S. Asano, A. Uchiyama, and A. Yamazaki, 2004: Seasonal variation of aerosol direct radiative forcing and optical properties estimated from ground-based solar radiation measurements. J. Atmos. Sci., 61, 57-72.

Novakov, T., V. Ramanathan, J. E. Hansen, T. W. Kirchstetter, M. Sato, and J. E. Sinton, 2003: Large historical changes of fossil-fuel black carbon aerosols. Geophys. Res. Lett., 30(6), doi: 10.1029/2002GL016345.

Quijano, A. L., I. N. Sokolik, and O. B. Toon, 2000; Radaitive heating rates and direct radiative forcing by mineral dust in cloudy atmospheric conditions. J. Geophys. Res.., 105(D10), 12207-12219.

Sud, Y. C. and G. K. Walker, 1999a: Mcrophysics of clouds with the relaxed Arakawa-Schubert scheme (McRAS). Part I: Design and evaluation with GATE phase III data. J. Atmos. Sci., 56, 3196-3220.

Sud, Y. C. and G. K. Walker, 1999b: Mcrophysics of clouds with the relaxed Arakawa-Schubert scheme (McRAS). Part II: Implementation and performance in GEOS II GCM. J. Atmos. Sci., 56, 3221-3240.

Sud, Y. C and G. K. Walker, 2003: New upgrades to the microphysics and thermodynamics of clouds in McRAS: SCM and GCM evalution of simulation biases in GEOS GCM. Proc. Indian Natn Sci. Acad, 69, 1, No. 5, 543-565.

Takemura, T., H. Okamoto, Y. Maruyama, A. Numaguti, A. Higurashi, and T. Nakagima. 2000: Global three-dimensional simulation of aerosol optical thickness distribution of various origins. J. Geophys. Res., 105, D14, 17853-17873.

Takemura, T., T. Nakajima, O. Bubovik, B. Holben, and S. Kinne, 2002a: Single scattering albedo and radiative forcing of various aerosol species with a global three dimensional model. J. of Climate, 15, 333-352.

Takemura, T., I. Uno, T. Nakajima, A. Higurashi, and I. Sano, 2002b: Modeling study of long-range transport of Asian dust and anthropogenic aerosols from East Asia. Geophy. Res. Let., 29(24), 10,1029/2002GL016251.

Tegen, I. and I. Fung, 1995: Contributions to the mineral acrosol load from land surface modification. J. Geophys. Res., 100, 18707-18726.

Tegen, I., A. Lacis, and I. Fung, 1996: The influence of mineral aerosol from distributed soils on the general radiation budget. Nature, 380, 419-422.

Weaver, C., P. Ginoux, N. C. Hsu, M. D. Chou, and J. Joiner, 2002: Radiative forcing of Saharan dust: GOCART model simulations compared with ERBE data. J. Atmos. Sci., 59, 736-747.

Wilks, D. S., 1995: Statistical methods in the atmospheric sciences. Academic press, 467pp.

Zhang, J., Y. Wu, C. L. Liu, Z. B. Shen, and Y. Zhang, 2002: Major components of aerosols in North China: Desert region and Yellow sea in the spring and summer of 1995 and 1996. J. Atmos. Sci., 59, 1515-1532.

Table 1 Global mean change induced by direct radiative forcing of five aerosols in spring. Positive (negative) values indicate the gain (loss) of energy, respectively.

	Shortwave flux	Longwave flux	Sensible heat flux	Latent heat flux	Net flux
Top of atmosphere	-1.1	-0.3	-	-	-1.4
Atmosphere	4.8	-1.2	-1.8	-1.5	0.3
Surface	-5.9	0.9	1.8	1.5	-1.7

Figure Caption

Fig. 1 Spatial pattern of long-term change in observed breal spring land surface temperature for the last 40 years. The change is calculated as the difference in mean between 1980-1998 and 1961-1979. Positive values over 0.8 ℃ per 20 years are shaded.

Fig.2 Distribution of GOCART aerosol optical thickness (AOT) in MAM of (a) all aerosols at wavelength of 0.55 μm. AOT of dust and black carbon is shown in (b) and (c), respectively. AOT of black carbon is scaled by a factor of 10. Regions over 0.4 are shaded. Contour intervals are 0.1.

Fig.3 Spatial distribution of monthly aerosol optical thickness (AOT) of (a) dust (upper), carbonaceous (middle), and sulfate (lower panel) aerosols at wavelength of 0.55 μm. The left, center, and right panels correspond to March, April, and May, respectively. Regions over 0.3 are shaded. Contour intervals are 0.1.

Fig.4 Latitude-height distributions of aerosol optical thickness at wavelength of 0.55 μm averaged between 0 -150° E for (a) all aerosols, (b) dust and (c) black carbon.. Contour intervals in (a), (b), and (c) are 10, 5, $1x10^{-4}$ mb^{-1}, respectively.

Fig.5 MAM aerosol radiative forcing (a) at the top of the atmosphere, (b) in the atmosphere, and (c) at the surface in Wm^{-2}, computed as the difference between the all-aerosol experiment and the control (AA-minus-NA). Contour intervals are 5 Wm^{-2}. Regions larger than 15 or smaller than -15 Wm^{-2} are shaded.

Fig. 6 MAM temperature anomaly induced by all aerosols at (a) 850hPa and (b) 500hPa. Significance levels of 5 % are shaded and contour intervals are 0.3℃.

Fig. 7 Spatial distribution of (a) Sea level pressure and (b) geopotential height anomaly

at 500hPa induced by all aerosols. Contour intervals in (a) and (b) are 0.5 hPa and 8 m, respectively

Fig. 8 Latitude-height distributions of meridional wind in (a) NA and (b) the meridional wind anomaly (AA-minus-NA) averaged over the 100-120°E longitude sector. Contour intervals are 1 for (a) and 0.3 ms^{-1} for (b), respectively. Latitude distribution of surface air temperature anomaly (solid line) and aerosol optical thickness (AOT) of sulfate (dotted line), dust (long dashed line), and carbonaceous aerosol (short dashed line) are indicated in (c).

Fig. 9 Latitude-height distribution of (a) temperature, (b) shortwave heating, (c) total diabatic heating, and (d) vertical pressure velocity anomaly induced by all aerosols averaged over the East Asian domain [100~120°E]. Contour intervals (a), (b), (c), and (d) are 0.2℃, 0.1 ℃ day^{-1}, 0.1℃ day^{-1}, and -0.3×10^{-4} hPa s^{-1}, respectively. In (d) negative anomaly denotes downward motion.

Fig. 10 Latitude-height distributions of meridional wind in (a) NA and (b) the meridional wind anomaly induced by all aerosols at 0-30°E. Contour intervals are 1 for (a) and 0.3 ms^{-1} for (b), respectively. Latitude distribution of surface air temperature anomaly (solid line) and aerosol optical thickness (AOT) of sulfate (dotted line), dust (long dashed line), and carbonaceous aerosol (short dashed line) are indicated in (c).

Fig. 11 Latitude-height distribution of (a) shortwave heating, (b) temperature, (c) diabatic heating, and (d) vertical pressure velocity anomaly induced by all aerosols at 0~30°E longitude band. Contour intervals (a), (b), (c), and (d) are 0.2℃, 0.1 ℃ day^{-1}, 0.1℃ day^{-1}, and -0.3×10^{-4} hPa s^{-1}, respectively. In (d), negative values denote anomalous sinking motion.

Fig. 12 MAM aerosol radiative forcing absorbed by the atmosphere by (a) all aerosols without dust (ND-minus-NA) and (b) all aerosols without BC (NB-minus- NA). Regions over 10 Wm^{-2} are shaded and contour intervals are 5 Wm^{-2}

Fig.13 MAM mean surface air temperature anomaly induced by (a) the effects of all aerosols (AA-NA), (b) dust aerosol with the background of four aerosols (AA-ND), and (c) BC aerosol with the background of four aerosols (AA-NB). Contour intervals are 0.5 ℃. Significance levels are shown in the half-tone scale on the right.

Fig.14 MAM temperature anomaly at 500hPa induced by (a) the effects of all aerosols (AA-minus-NA), (b) dust aerosol with the background of four aerosols (AA-minus-ND), and (c) BC aerosol with the background of four aerosols (AA-minus-NB). Contour intervals are 0.5 ℃. Statistical significant levels are shown in the half-tone scale on the right.

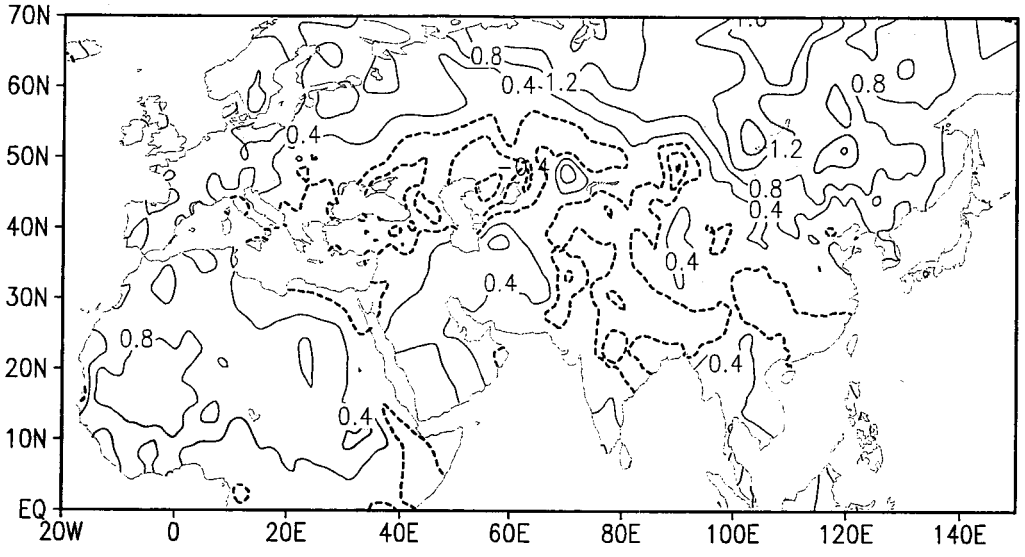

Fig. 1 Spatial pattern of long-term change in observed boreal spring land surface temperature for the last 40 years. The change is calculated as the difference in mean between 1980-1998 and 1961-1979. Positive values over 0.8 ℃ per 20 years are shaded.

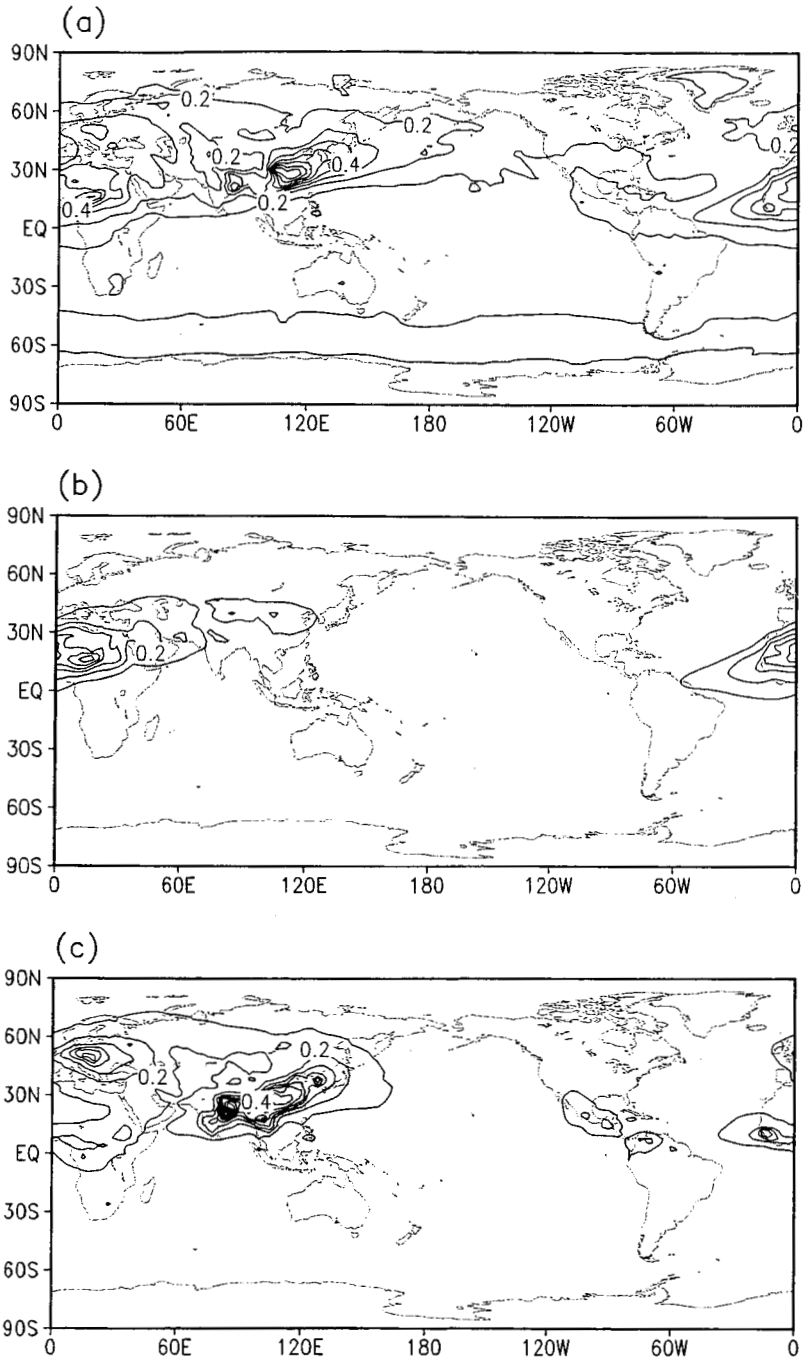

Fig.2 Distribution of GOCART aerosol optical thickness (AOT) in MAM of (a) all aerosols at wavelength of 0.55 μm. AOT of dust and black carbon is shown in (b) and (c), respectively. AOT of black carbon is scaled by a factor of 10. Regions over 0.4 are shaded. Contour intervals are 0.1.

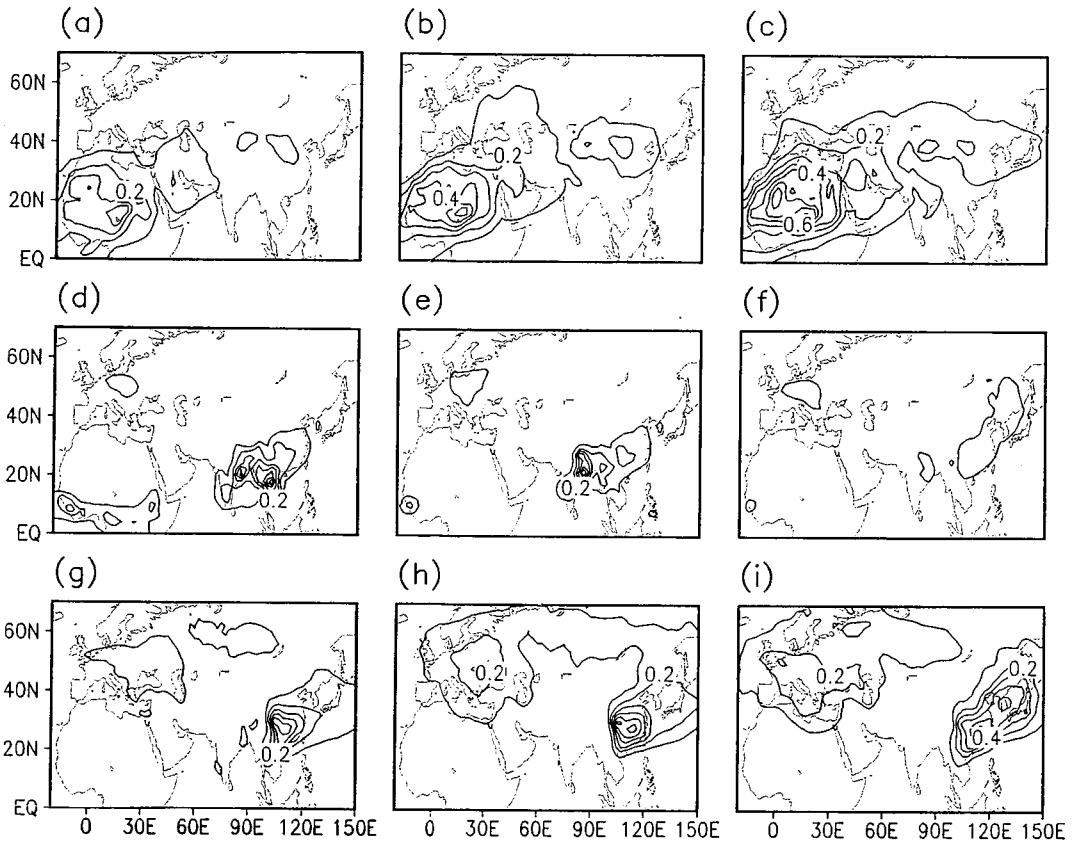

Fig.3 Spatial distribution of monthly aerosol optical thickness (AOT) of (a) dust (upper), carbonaceous (middle),and sulfate (lower panel) aerosols at wavelength of 0.55 μm. The left, center, and right panels correspond to March, April, and May, respectively. Regions over 0.3 are shaded. Contour intervals are 0.1.

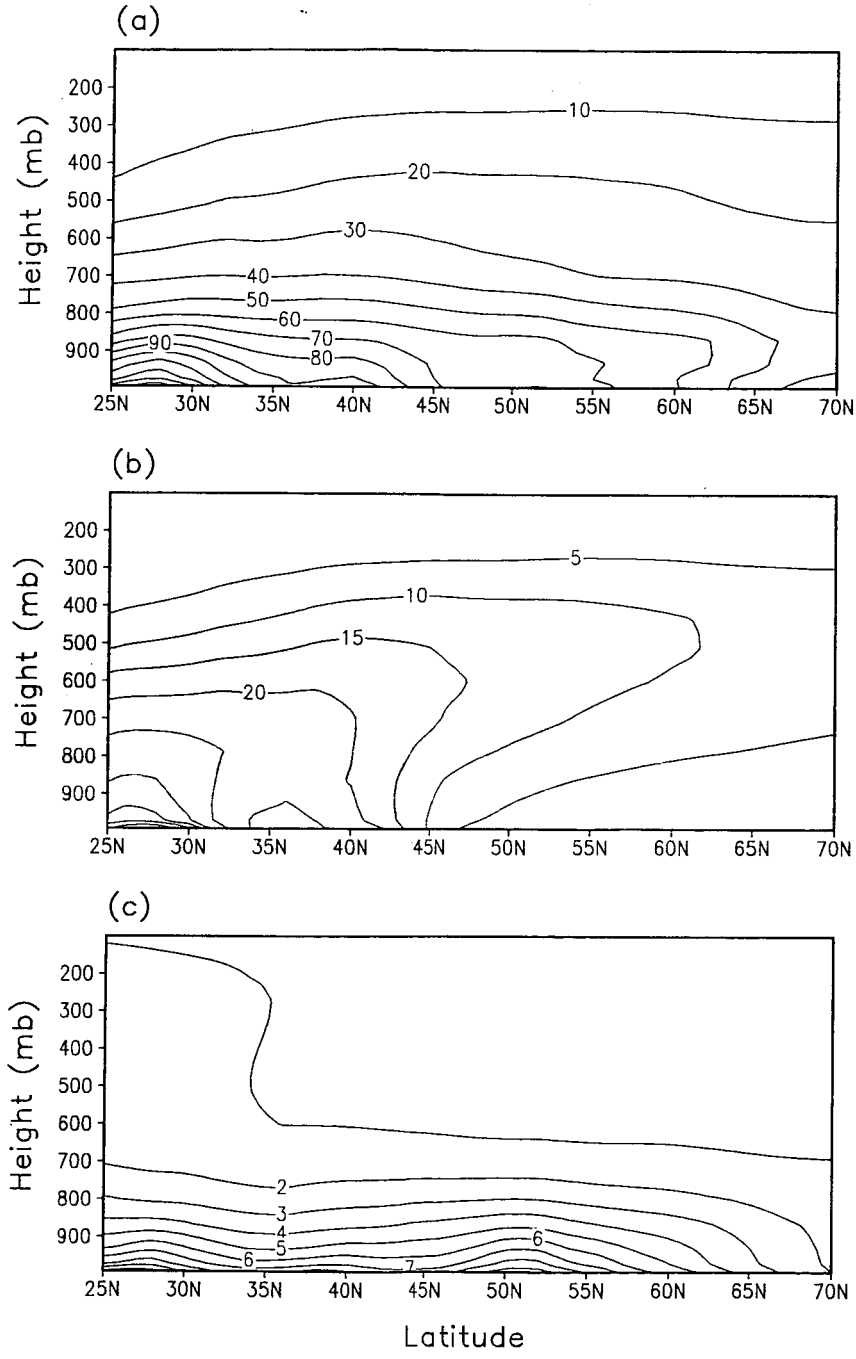

Fig.4 Latitude-height distributions of aerosol optical thickness at wavelength of 0.55 μm averaged between 0 -150° E for (a) all aerosols, (b) dust and (c) black carbon.. Contour intervals in (a), (b), and (c) are 10, 5, $1x10^{-4}$ mb^{-1}, respectively.

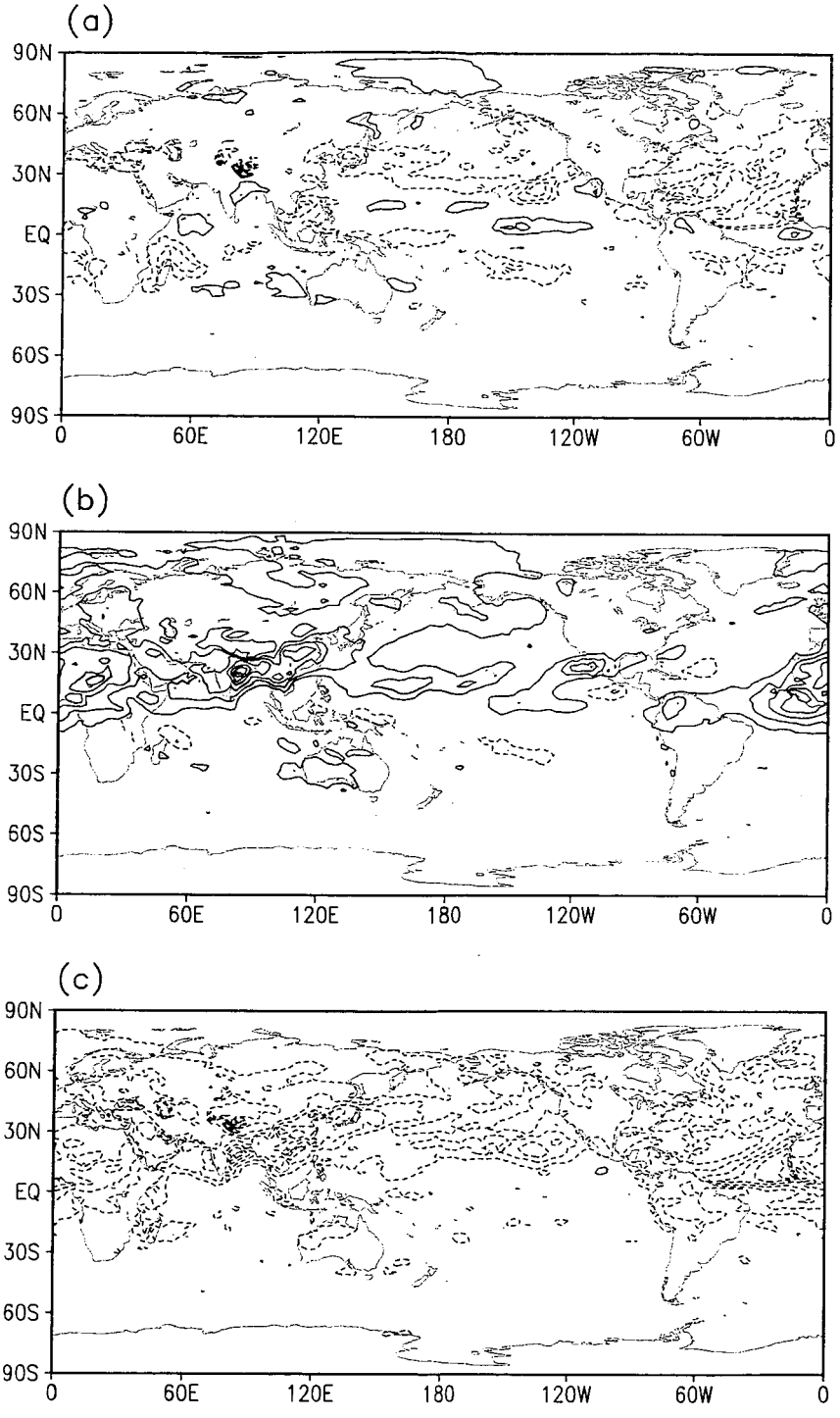

Fig.5 Aerosol radiative forcing (a) at the top of the atmosphere, (b) in the atmosphere, and (c) at the surface in Wm^{-2}, computed as the difference between the all-aerosol experiment and the control (AA-minus-NA). Contour intervals are 5 Wm^{-2}. Regions larger than 15 or smaller than -15 Wm^{-2} are shaded.

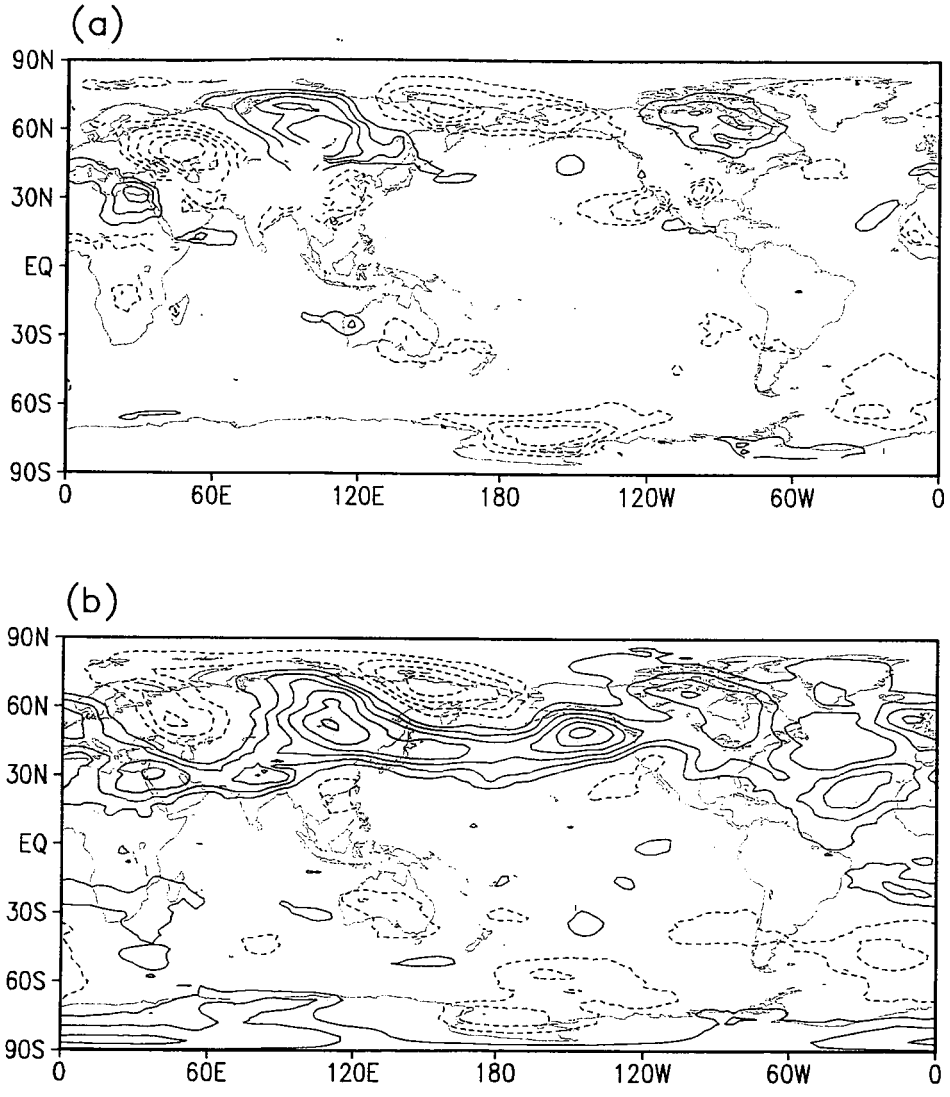

Fig. 6 MAM temperature anomaly induced by all aerosols at (a) 850hPa and (b) 500hPa. Significance levels of 5 % are shaded and contour intervals are 0.3℃.

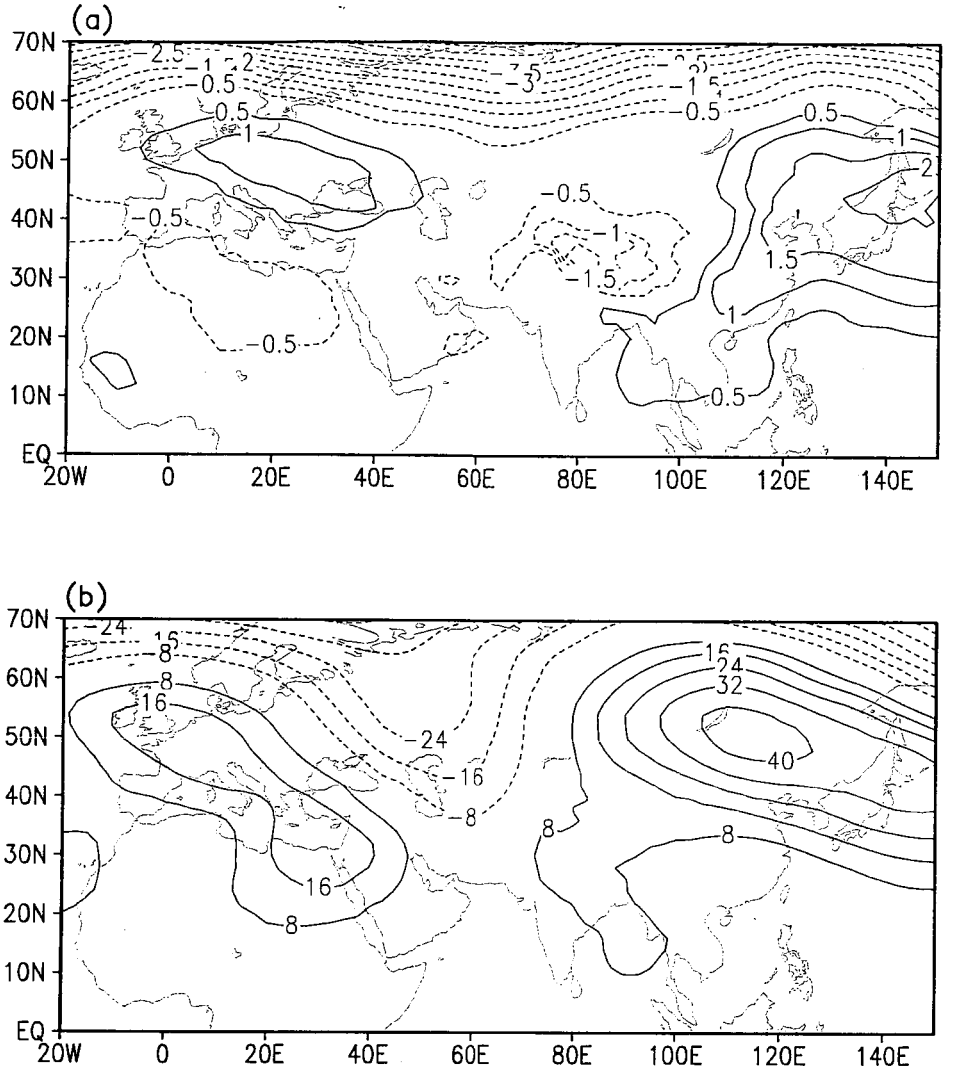

Fig. 7 Spatial distribution of (a) Sea level pressure and (b) geopotential height anomaly at 500hPa induced by all aerosols. Contour intervals in (a) and (b) are 0.5 hPa and 8 m, respectively.

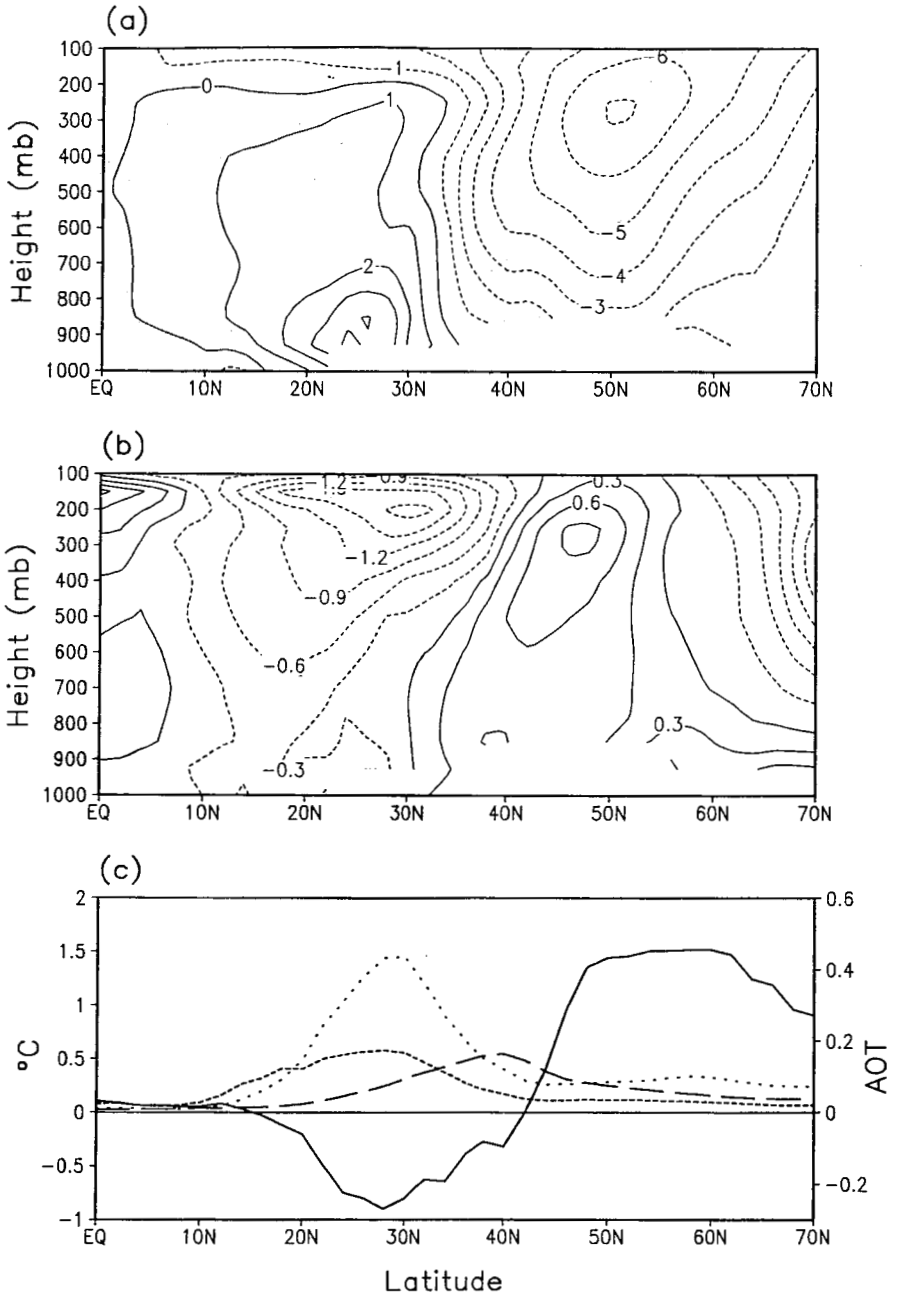

Fig. 8 Latitude-height distributions of meridional wind in (a) NA and (b) the meridional wind anomaly (AA-minus-NA) averaged over the 100-120°E longitude sector. Contour intervals are 1 for (a) and 0.3 ms^{-1} for (b), respectively. Latitude distribution of surface air temperature anomaly (solid line) and aerosol optical thickness (AOT) of sulfate (dotted line), dust (long dashed line), and carbonaceous aerosol (short dashed line) are indicated in (c).

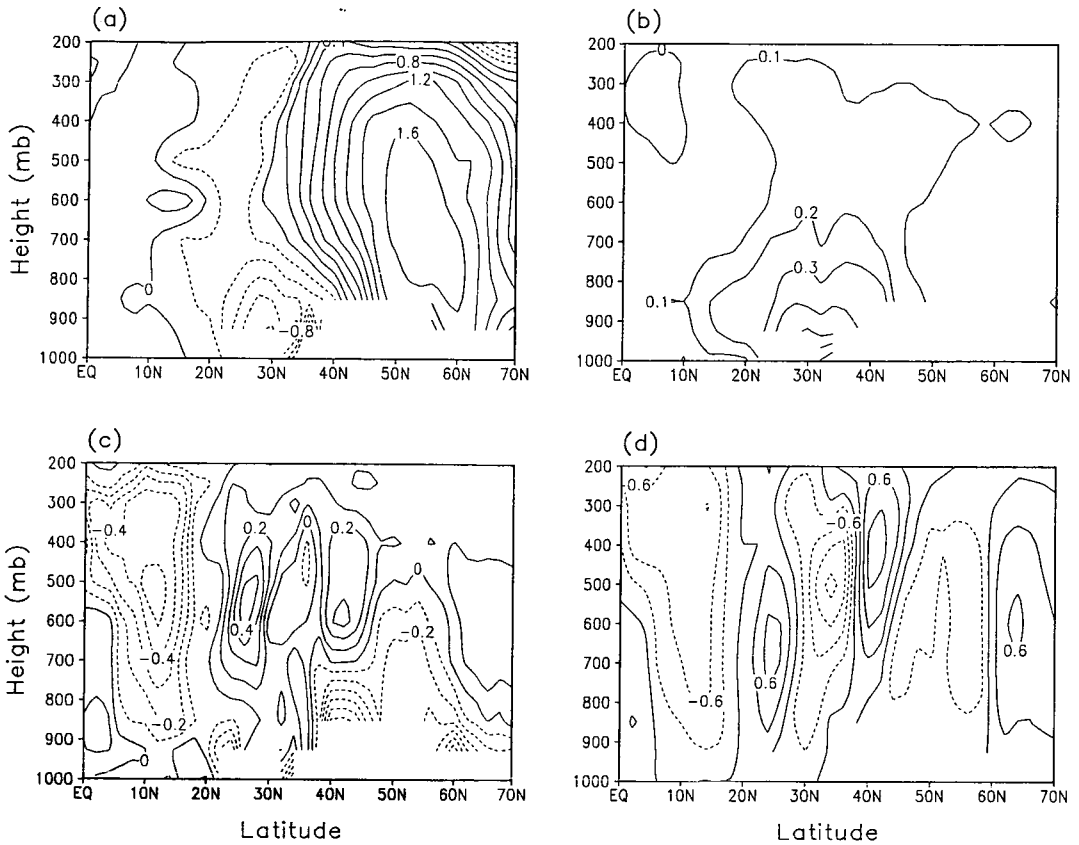

Fig. 9 Latitude-height distribution of (a) temperature, (b) shortwave heating, (c) total diabatic heating, and (d) vertical pressure velocity anomaly induced by all aerosols averaged over the East Asian domain [100~120°E]. Contour intervals (a), (b), (c), and (d) are 0.2℃, 0.1 ℃ day^{-1}, 0.1℃ day^{-1}, and -0.3×10^{-4} hPa s^{-1}, respectively. In (d) negative anomaly denotes downward motion.

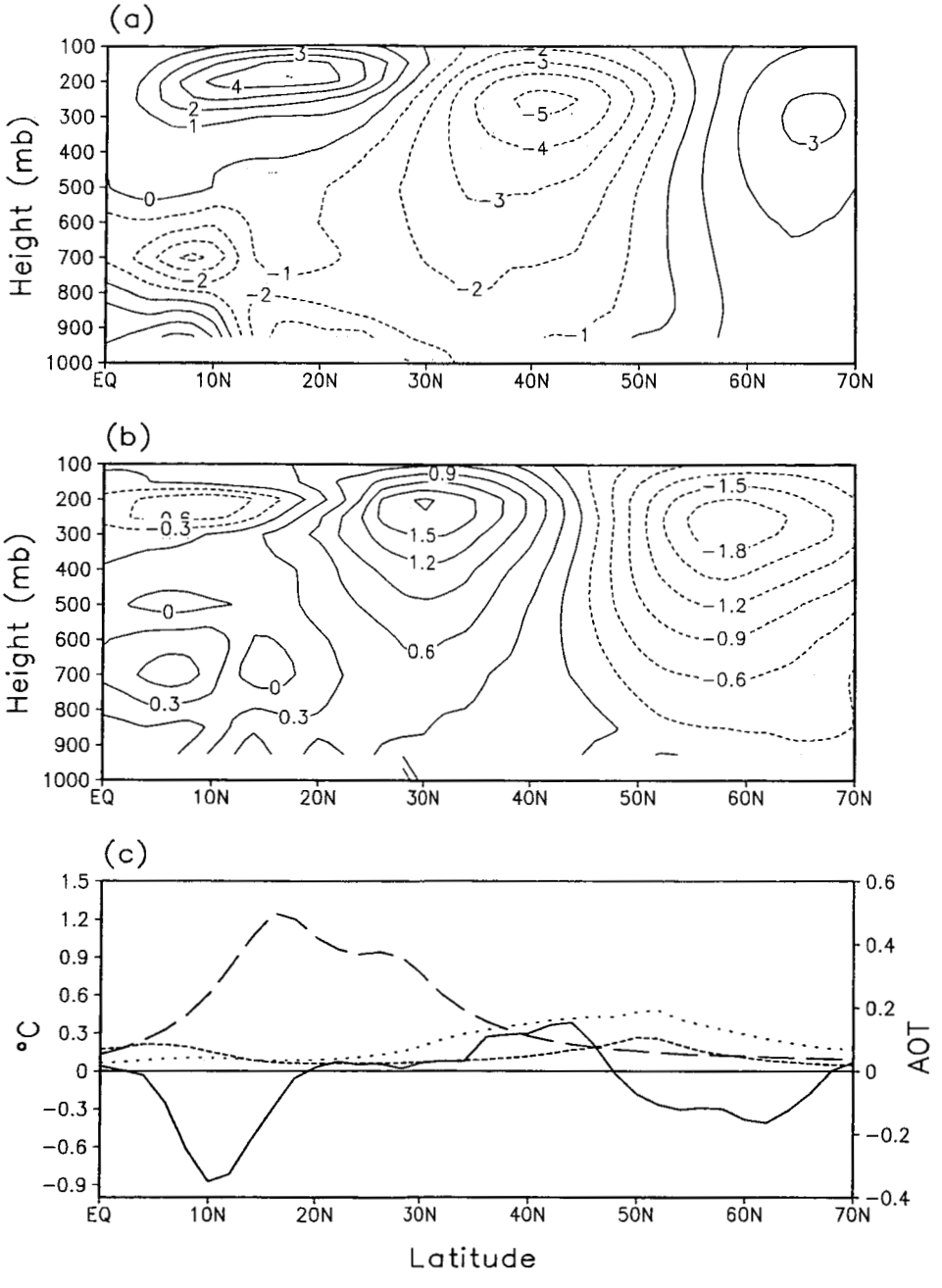

Fig. 10 Latitude-height distributions of meridional wind in (a) NA and (b) the meridional wind anomaly induced by all aerosols at 0-30°E. Contour intervals are 1 for (a) and 0.3 ms^{-1} for (b), respectively. Latitude distribution of surface air temperature anomaly (solid line) and aerosol optical thickness (AOT) of sulfate (dotted line), dust (long dashed line), and carbonaceous aerosol (short dashed line) are indicated in (c).

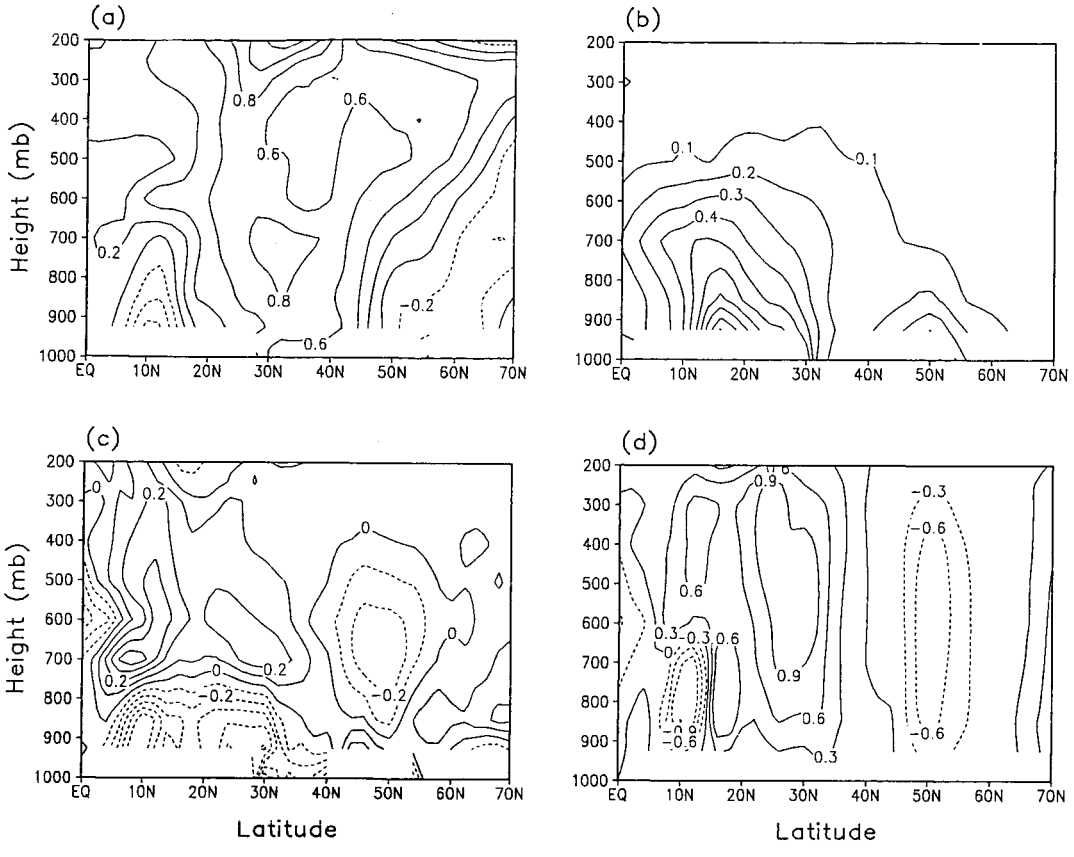

Fig. 11 Latitude-height distribution of (a) shortwave heating, (b) temperature, (c) diabatic heating, and (d) vertical pressure velocity anomaly induced by all aerosols at 0~30°E longitude band. Contour intervals (a), (b), (c), and (d) are 0.2℃, 0.1 ℃ day^{-1}, 0.1℃ day^{-1}, and -0.3×10^{-4} hPa s^{-1}, respectively. In (d), negative values denote anomalous sinking motion.

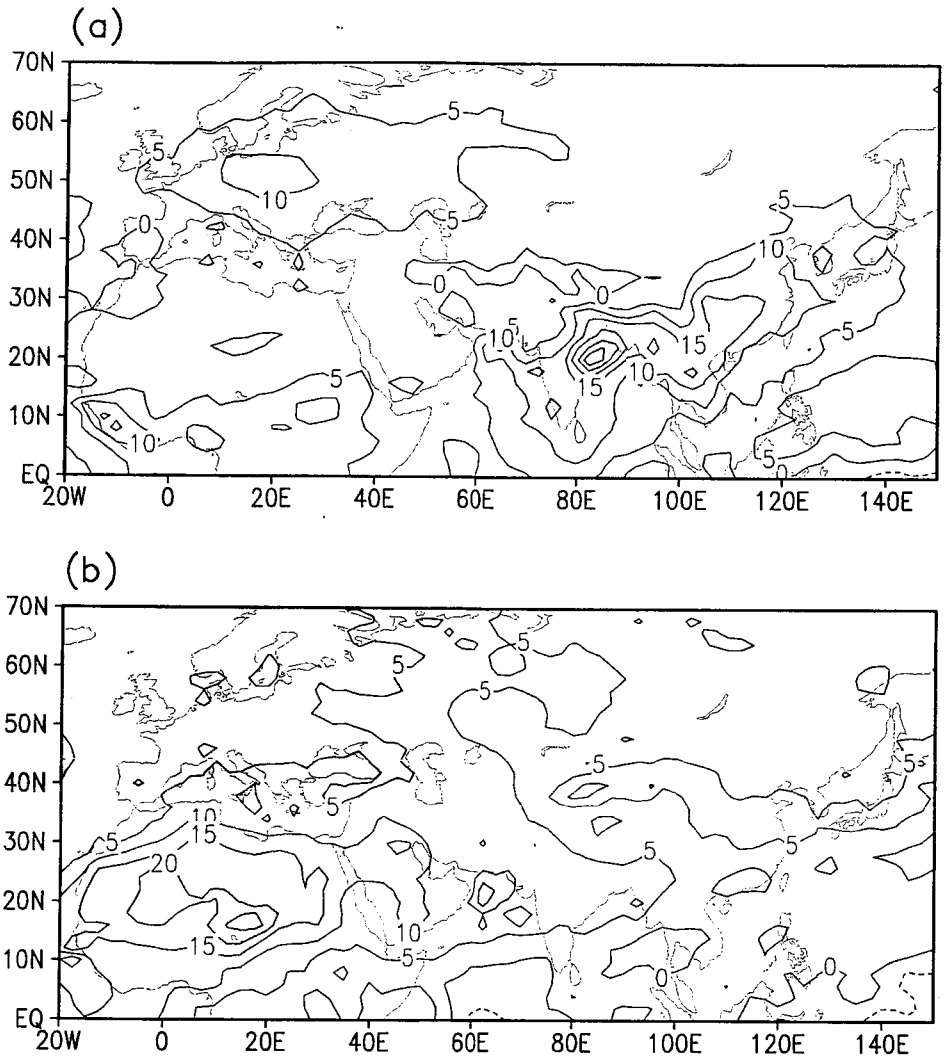

Fig. 12 MAM aerosol radiative forcing absorbed by the atmosphere by (a) all aerosols without dust (ND-minus-NA) and (b) all aerosols without BC (NB-minus- NA). Regions over 10 Wm^{-2} are shaded and contour intervals are 5 Wm^{-2}.

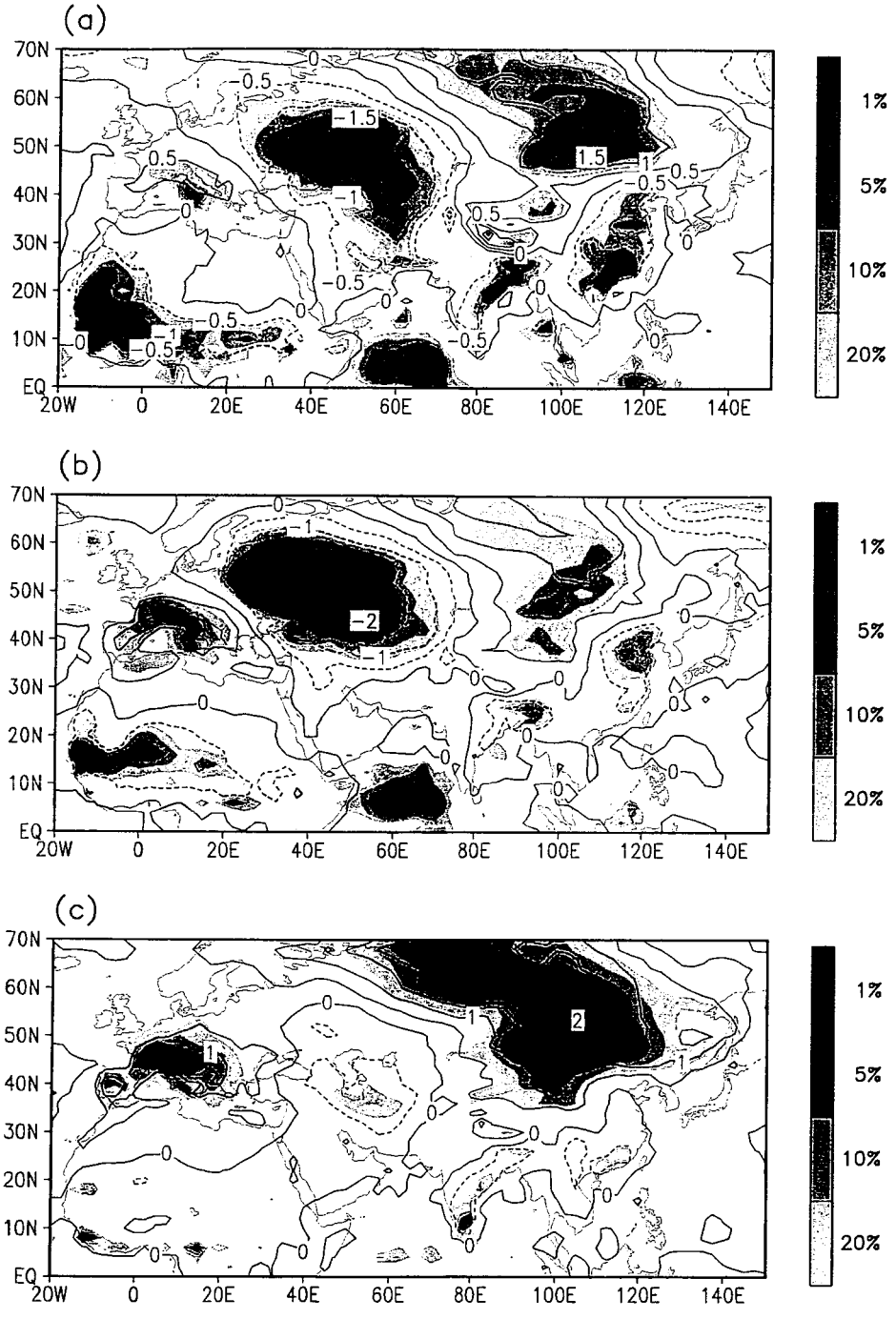

Fig. 13 MAM mean surface air temperature anomaly induced by (a) the effects of all aerosols (AA-NA), (b) dust aerosol with the background of four aerosols (AA-ND), and (c) BC aerosol with the background of four aerosols (AA-NB). Contour intervals are 0.5 ℃. Significance levels are shown as half-tone scale on the right.

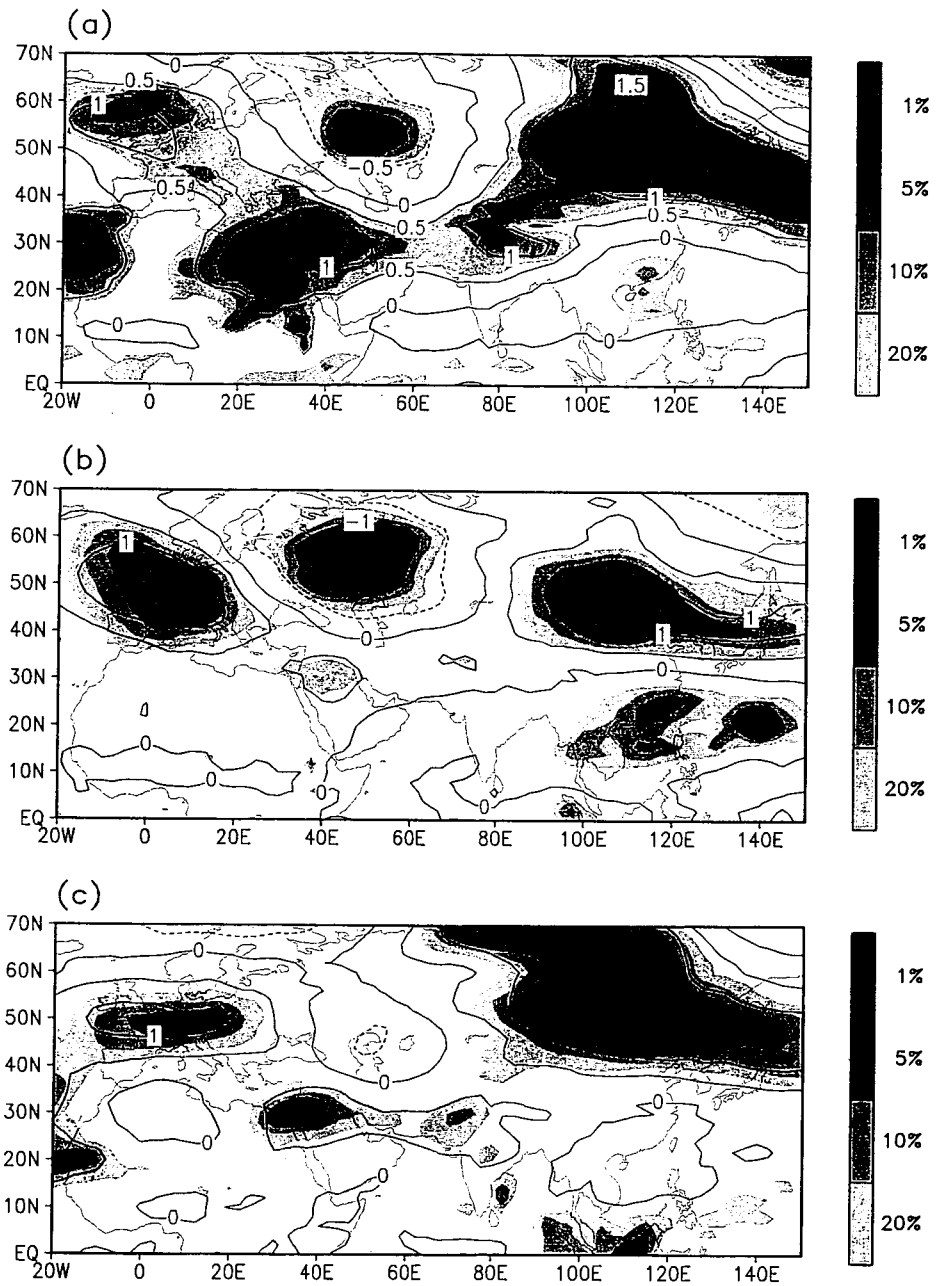

Fig.14 MAM temperature anomaly at 500hPa induced by (a) the effects of all aerosols (AA-minus-NA), (b) dust aerosol with the background of four aerosols (AA-minus-ND), and (c) BC aerosol with the background of four aerosols (AA-minus-NB). Contour intervals are 0.5 ℃. Statistical significant levels are shown in the half-tone scale on the right.

Popular Summary

Aerosols refer to small suspended particles, typically of the size less than one-hundredth of the diameter of a human hair. They are derived from a variety of sources such as industrial pollution, biomass burning, desert dust, volcanic eruptions, and sea salt from ocean wave spray. Aerosols are well known as a leading environmental hazard in causing health problems, and in reducing visibility. Not so well known, is that aerosols also play an important role in regulating the global water cycle and climate. Depending on their compositions, aerosols can reflect or absorbing sunlight, thus cooling or heating the atmosphere. Whether through absorption or reflection, aerosols always reduce sun light reaching the surface and cause the surface to cool. In addition, aerosols facilitate the formation of clouds by providing cloud condensation nuclei so that water vapor in the atmosphere can readily condense into cloud drops. Hence more aerosols will mean more clouds. Furthermore clouds drop formed from aerosols, tend to stay in the atmosphere longer because the drops are smaller. Because smaller drops have less chance to collide and to coalesce to form into larger rain drops, aerosols suppress rain formation. Under other circumstances, aerosols may also enhance rainfall. Most important, all the aforementioned processes will produce heating gradients in the vertical and horizontal, that drive changes in the large scale circulation, which then alter the aerosol distribution through transport, deposition and chemical interactions. The interactions of aerosol, clouds, precipitation and the large scale circulation are extreme complex and not well understood.

In this paper, we investigate one aspect, i.e., the direct heating effects, induced by aerosols on global and regional climate during boreal spring We find that anomalous atmospheric heat sources induced by absorbing aerosols (dust and black carbon) excites a planetary scale teleconnection pattern in sea level pressure, temperature and geopotential height spanning North Africa through Eurasia to the North Pacific. Surface cooling due to direct effects of aerosols is found in the vicinity and downstream of the aerosol source regions, i.e., South Asia, East Asia, and northern and western Africa. Additionally, atmospheric heating is found in regions with large loading of dust (over Northern Africa, and Middle East), and black carbon (over South-East Asia). Paradoxically, the most pronounced feature in aerosol-induced surface temperature is an east-west dipole anomaly with strong cooling over the Caspian Sea, and warming over central and northeastern Asia, where aerosol concentration are low. Analyses of circulation anomalies show that the dipole anomaly is a part of an atmospheric teleconnection driven by atmospheric heating anomalies induced by absorbing aerosols in the source regions, but the influence was conveyed globally through barotropic energy dispersion and sustained by feedback processes associated with the regional circulations. Atmospheric heating by dust aerosol over northern Africa and the Middle East is the primary driver of the atmospheric teleconnection, with significant contribution by black carbon over South and East Asia. The results of this paper demonstrate that aerosols effects are not only region, but also global invoking feedback processes of the entire global general circulation.